Earth and Planetary Science Letters 430 (2015) 499–510

Contents lists available at ScienceDirect

Earth and Planetary Science Letters

www.elsevier.com/locate/epsl

Coupled measurements of $\delta^{18}O$ and δD of hydration water and salinity of fluid inclusions in gypsum from the Messinian Yesares Member, Sorbas Basin (SE Spain)

Nicholas P. Evans [a,*], Alexandra V. Turchyn [a], Fernando Gázquez [a], Tomaso R.R. Bontognali [b], Hazel J. Chapman [a], David A. Hodell [a]

[a] Godwin Laboratory for Palaeoclimate Research, Department of Earth Sciences, University of Cambridge, Downing Street, Cambridge, CB2 3EQ, United Kingdom
[b] ETH-Zurich, Geological Institute and Institute of Geochemistry and Petrology, Sonneggstrasse 5, Zurich 8092, Switzerland

ARTICLE INFO

Article history:
Received 10 March 2015
Received in revised form 30 July 2015
Accepted 31 July 2015
Available online 28 August 2015
Editor: H. Stoll

Keywords:
gypsum hydration water
fluid inclusions
Messinian salinity crisis
Mediterranean
evaporites
cyclostratigraphy

ABSTRACT

We studied one cycle (Cycle 6) of gypsum–marl deposition from the Messinian Yesares Member in Sorbas Basin, Spain. The objective was to reconstruct the changing environment of deposition and its relation to astronomically-forced climate change. The $\delta^{18}O$ and δD of gypsum hydration water ($CaSO_4 \bullet 2H_2O$) and salinity of fluid inclusions were measured in the same samples to test if they record the composition of the mother fluid from which gypsum was precipitated. Water isotopes are highly correlated with fluid inclusion salinity suggesting the hydration water has not exchanged after formation. The relatively low water isotope values and fluid inclusion salinities indicate a significant influence of meteoric water, whereas $\delta^{34}S$, $\delta^{18}O_{SO_4}$ and $^{87}Sr/^{86}Sr$ support a dominant marine origin for the gypsum deposits. The discrepancy between water and elemental isotope signatures can be reconciled if meteoric water dissolved previously deposited marine sulfates supplying calcium and sulfate ions to the basin which maintained gypsum saturation. This recycling process accounts for the marine $\delta^{34}S$, $\delta^{18}O_{SO_4}$ and $^{87}Sr/^{86}Sr$ signatures, whereas the low $\delta^{18}O$ and δD values of gypsum hydration water and fluid inclusion salinities reflect the influence of freshwater.

The cyclic deposition of gypsum and marl in the Yesares Member has previously been interpreted to reflect changing climate related to Earth's precession cycle. We demonstrate that the $\delta^{18}O$, δD and salinity of the parent brine increased from low values at the base of the cycle to a maximum in the massive gypsum palisade, and decreased again to lower values in the supercones at the top of the cycle. This pattern, together with changes in mineralogy (calcite–dolomite–gypsum), is consistent with a precession-driven change in climate with wettest conditions (summer insolation maxima) associated with the base of the calcium carbonate marls and driest conditions (summer insolation minima) during formation of the gypsum palisade.

1. Introduction

During the Messinian salinity crisis (MSC), the Mediterranean Sea was transformed into a giant brine pool where more than one million cubic kilometers of salt was deposited in 630 ka (Fig. 1) (Krijgsman et al., 1999; Rouchy and Caruso, 2006; Manzi et al., 2012). Most of the deposits in the deep-basins have remained unsampled; thus, studies have relied upon onshore Messinian deposits in marginal basins to infer the stratigraphic history of the MSC (Roveri et al., 2014a).

In marginal basins of the circum-Mediterranean, the lowermost gypsum bed marking the onset of the MSC is dated at ~5.97 Ma (Krijgsman et al., 1999; Manzi et al., 2013). The overlying unit known as the *Primary Lower Gypsum* comprises up to 16 beds of massive gypsum interbedded with finely laminated marls or shale (Roveri et al., 2009; Lugli et al., 2010). The deposition of these evaporite–marl cycles is reported to be controlled by the variations of Earth's orbital parameters, mainly the ~21-kyr precession cycle (Krijgsman et al., 1999, 2001; Lugli et al., 2010; Manzi et al., 2009, 2012). According to this interpretation, evaporite deposition occurred at the precession maxima (i.e. minimum summer insolation when summer solstice and aphelion coincided) when evaporation exceeded precipitation during periods of dry climate and marl deposition occurred at precession minima (maximum sum-

* Corresponding author.
E-mail address: ne243@cam.ac.uk (N.P. Evans).

http://dx.doi.org/10.1016/j.epsl.2015.07.071

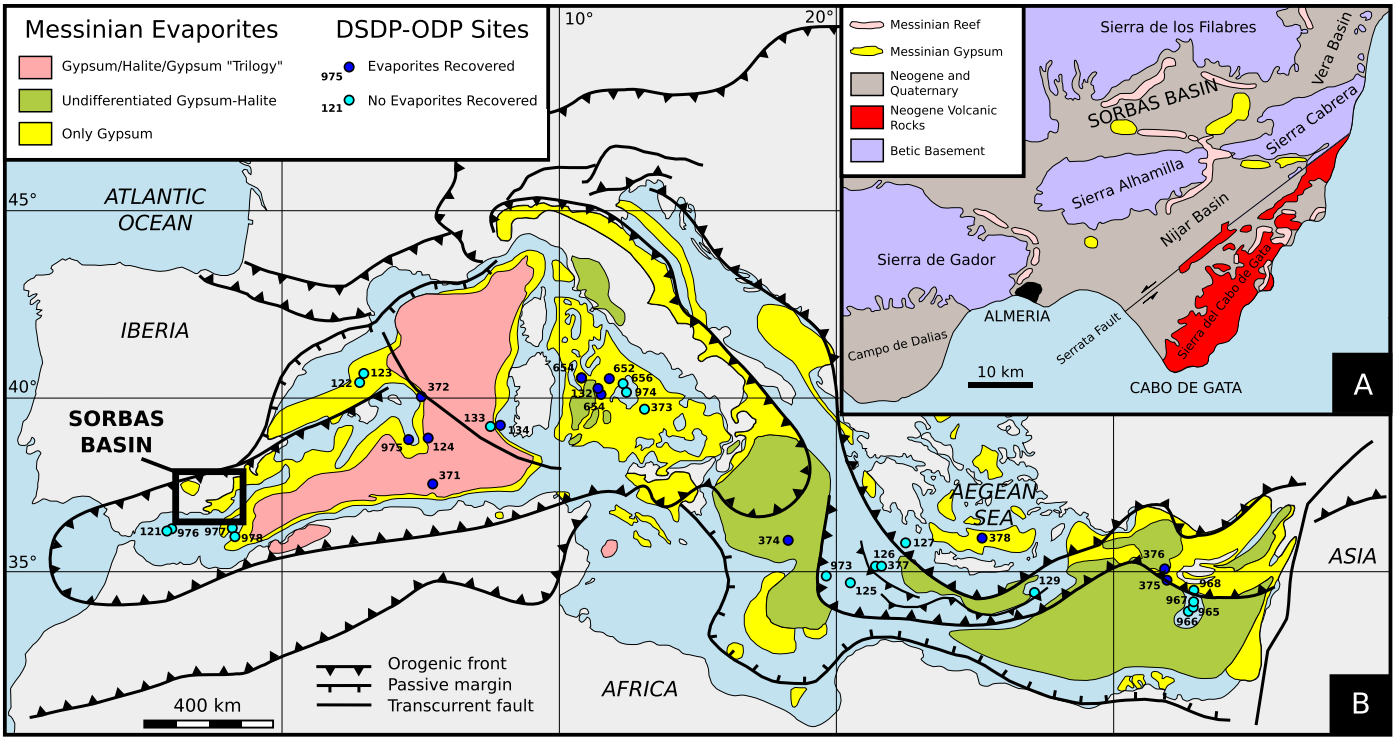

Fig. 1. (**A**) Location map of the Sorbas Basin and surrounding areas modified after Krijgsman et al. (2001). Indicated are the distributions of the outcropping marginal Messinian reefs (Cantera Member) and gypsum deposits (Yesares Member). (**B**) Map of the Messinian evaporites in the Mediterranean modified after Rouchy and Caruso (2006) and Roveri et al. (2014a). Also shown is the location of the DSDP-ODP boreholes in which Messinian evaporites were recovered.

mer insolation when summer solstice and perihelion coincided) when rainfall increased (Krijgsman et al., 1999, 2001).

Whereas orbital forcing may explain the observed large-scale lithological cyclicity, the composition and salinity of the brines from which large volumes of sulfate minerals formed are still debated. Most information on brine chemistry has been inferred using strontium ($^{87}Sr/^{86}Sr$), sulfur ($\delta^{34}S$), and oxygen isotopes in sulfate ($\delta^{18}O_{SO_4}$) (e.g., Longinelli, 1979; Müller and Mueller, 1991; Lu and Meyers, 2003; Lugli et al., 2007, 2010). Here we combine these traditional isotope tracers with the measurement of gypsum hydration water and fluid inclusions to reconstruct the chemical composition of the parent brine solution.

The measurement of oxygen and hydrogen isotopes in gypsum hydration water is a potentially powerful tool for studying the nature of the parent water from which gypsum was precipitated (Sofer, 1978; Longinelli, 1979; Hodell et al., 2012). An assumption of the method is that once formed, gypsum hydration water retains its isotope composition and does not undergo postdepositional isotopic exchange (Sofer, 1978). To test this assumption, we compare the isotope composition of the hydration with the salinity of fluid inclusions in gypsum estimated by microthermometry (Goldstein and Reynolds, 1994; Attia et al., 1995; Natalicchio et al., 2014). We expect the $\delta^{18}O$ and δD of hydration water to be well correlated with the salinity of primary fluid inclusions if it has retained the isotopic signature of the mother water.

In addition to $^{87}Sr/^{86}Sr$, $\delta^{34}S$, and $\delta^{18}O_{SO_4}$ isotope analysis of gypsum, we measured oxygen and hydrogen isotopes in gypsum hydration water and salinity of fluid inclusions in gypsum from the sixth cycle of gypsum deposition from the Río de Aguas section, Sorbas Basin. We also measured modern gypsum deposits from the Cabo de Gata Salina, Almería, Spain, to provide a comparison to Messinian gypsum. We demonstrate that the hydration water in Messinian gypsum of Sorbas Basin has retained its original isotopic composition and can be used to infer paleoenvironmental conditions of gypsum deposition. We also show a well-defined cyclicity in the mineralogy and $\delta^{18}O$ and δD of gypsum hydration water and fluid inclusion salinity over a single gypsum cycle that is consistent with astronomical forcing of Messinian climate.

2. Geological setting

The Neogene Sorbas Basin in southeastern Spain is an elongated intra-montane depression surrounded by basement highs of the Betic Internal Zone (Fig. 1A). The deposition of evaporites begins with gypsum/marl cycles of the basal Yesares Member. These evaporites consist of gypsum deposits that are interbedded with laminated marls. The Yesares Member consists of a total of 16 gypsum cycles and is best exposed in the Río de Aguas section in the Sorbas Basin (Krijgsman et al., 2001; Roveri et al., 2009).

The stratigraphy of the Río de Aguas section was described by Dronkert (1977; 1985) and, more recently, by Lugli et al. (2010). Cycle 6 at the base of the Río de Aguas section (Fig. 2) begins in the marl that underlies the gypsum (Krijgsman et al., 2001). Lugli et al. (2010) identified this bed as Cycle 8, but, for identification purposes only, we have retained the original cycle designation as 6. The contact between the marl and overlying gypsum is undulating containing structures interpreted to be “nucleation cones” (Dronkert, 1985). These load structures consist of conical clusters of crystals that occur at the base of the gypsum beds, representing the initial nucleation points of gypsum that sank into the relatively soft marls (Lugli et al., 2010). The lower part of the gypsum unit consists of massive, vertically-elongated, twinned (“selenite”) crystals described as “arrow-headed” or “swallow-tailed” (Bąbel, 2004; Lugli et al., 2010). The crystals have a preferred vertical orientation and produce a “palisade”-like structure (Dronkert, 1985). The base of the gypsum beds generally consists of the largest crystals (up to 20 cm in length) and the size become progressively smaller (up to a few centimeters) up section.

Between 1 and 2 m above the base of the gypsum layer (average ~130 cm), crystal size decreases and is described as “banded

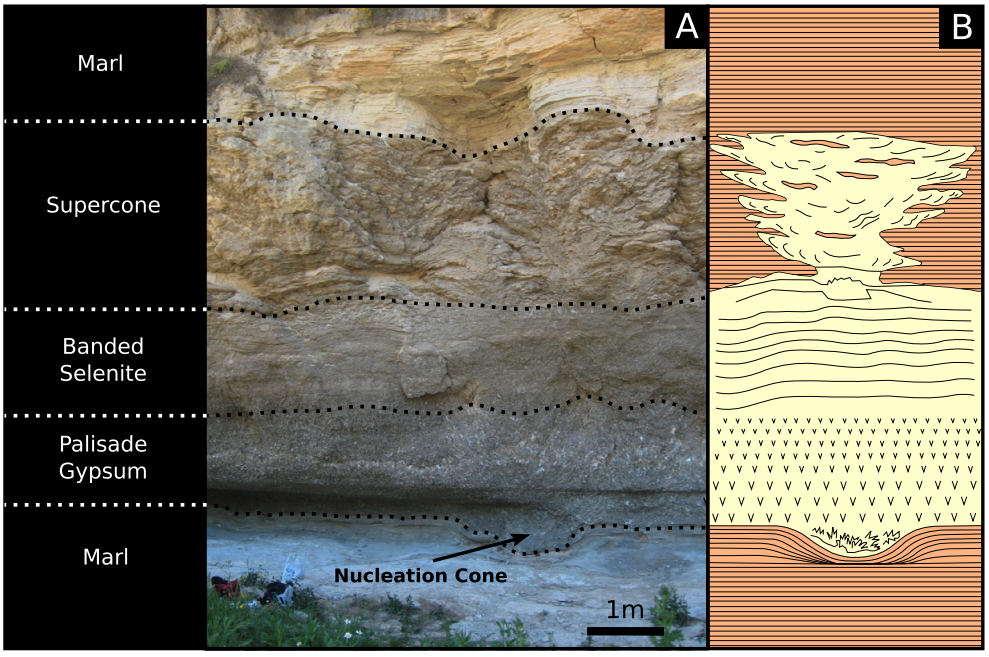

Fig. 2. Cycle 6 of the Río de Aguas section, displaying the differing crystal morphology and structures (**A**) relative to a schematic diagram (**B**) (after Dronkert, 1977). Carbonate marls occur at the onset and termination of the cycle. Nucleation cones represent the onset of gypsum precipitation. Palisade gypsum directly above the nucleation cones contains large, vertically orientated selenite crystals. Selenite palisade is overlain by banded selenite that are, in turn, overlain by asymmetric conical structure (supercones) juxtaposed to carbonate marls.

selenite" (Lugli et al., 2010). Above the banded selenite, the gypsum grades into giant cauliflower-shaped "supercones" (Dronkert, 1985). The occurrence of this branching selenite facies (Lugli et al., 2010) from the 6th Cycle upwards is of particular importance as it provides a marker bed for correlation to other sections across the Mediterranean (Roveri et al., 2014a). Supercone structures are created from clusters of small gypsum crystals creating curved, horizontal branches up to ~2 m in length. The branches originate from a central nucleation region and gradually increase in length towards the top of the section, thus forming the inverted cauliflower-shaped cones (Dronkert, 1977; Lugli et al., 2010). Laminated marls occur in pods between the branches of the supercones and carbonate minerals are composed almost entirely of dolomite. Some of the carbonate laminae can be traced into the gypsum crystals where they thin and disappear, indicating the gypsum and marl are syndepositional.

3. Methods

3.1. Field locations and sample collection methods

We sampled gypsum Cycle 6 that is exposed at the base of the Río de Aguas section (37°05′23.2″N 002°06′54.2″W) in Sorbas Basin, SE Spain (Dronkert, 1985; Krijgsman et al., 2001). Samples were collected in April 2013 and March 2014. The zero depth reference was taken as the horizontal base of the palisade gypsum layer; therefore, gypsum crystals sampled in nucleation cones have a negative depth reference. Marl samples were obtained from the base of the section and from marls juxtaposed to the supercones. See Supplementary Information (SI) and SI Figs. 1 and 2 for details of the sample collection.

3.2. $\delta^{34}S$ and $\delta^{18}O$ of sulfate

Samples for isotope analysis were ground to a fine powder, dissolved in deionized water and reprecipitated as barite (barium sulfate – $BaSO_4$). Prior to analysis they were cleaned in 6N HCl and rinsed in deionized water to purify the barite from any co-precipitating minerals. For $\delta^{18}O_{SO_4}$ analysis, barite was pyrolyzed at 1450 °C in a Temperature Conversion Element Analyzer (TC/EA), and the resulting carbon monoxide (CO) was measured by continuous flow isotope ratio mass spectrometry (IRMS) with a ThermoFisher Delta V Plus. For the $\delta^{34}S$ analysis, the barite was combusted at 1030 °C in a Flash Element Analyzer (EA), and the resulting sulfur dioxide (SO_2) was measured by continuous flow IRMS (Delta V Plus). Samples were run in triplicate for $\delta^{18}O_{SO_4}$ and the average and standard deviation of these replicate analyses is presented. Samples were bracketed by NBS127, an international barite standard, which was corrected to $\delta^{18}O_{SO_4}$ of 8.6‰ and $\delta^{34}S$ of 20.3‰.

3.3. Sr isotopes of gypsum

Approximately 10 mg of powdered gypsum was processed for strontium isotopic analysis. Strontium was separated by standard cation exchange chemistry. Strontium isotopic ratios were determined on a VG Sector thermal ionization mass-spectrometer (see SI for details). The internal standard NBS 987 gave 0.710257 ± 0.000010 (1σ) on 45 separate measurements over the last two years. Procedural blanks for strontium were negligible.

3.4. X-ray diffraction (XRD)

XRD data were used to estimate the relative proportion of calcite to dolomite in the sample. Samples were ground to <5 μm particles, slurry mounted onto glass slides with acetone, and analyzed with a D8 Bruker diffractometer (see SI for details).

3.5. Total inorganic carbon, $\delta^{18}O_{carb}$ and $\delta^{13}C$ of bulk carbonates

Samples were digested in 50% H_3PO_4 for 20 hours at 70 °C and total inorganic carbon was measured using an AutoMateFX autosampler coupled to a UIC (Coulometrics) 5011 CO_2 coulometer (Engleman et al., 1985). Analytical precision was estimated by

analysis of reagent-grade $CaCO_3$ (100%) and $MgCa(CO_3)_2$ (100%) and yielded a mean and 1σ standard deviation of $99.5 \pm 0.4\%$ and $94.6 \pm 0.8\%$ for calcite and dolomite, respectively. The dolomite is likely underestimate because of incomplete reaction even after 20 h. Weight %calcite and dolomite of samples were calculated using the dolomite/calcite ratio obtained by XRD multiplied by the total inorganic carbon measured by coulometric titration. Results are expressed as weight $\%CaCO_3$ and weight $\%MgCa(CO_3)_2$ assuming typical stoichiometry.

For stable isotope analysis, bulk sediment samples were ground to a fine powder, flushed with CP grade helium then acidified with 104% H_3PO_4 and left to react for 1 h at 70 °C. Stable carbon and oxygen isotopes of carbonate were measured using a ThermoScientific GasBench II, equipped with a CTC autosampler coupled to a MAT253 mass spectrometer (Spötl and Vennemann, 2003). Analytical precision was estimated at ±0.08‰ for $\delta^{13}C$ and ±0.1‰ for $\delta^{18}O_{carb}$ by repeated analysis of the Carrara Marble standard. Results are reported relative to the Vienna Pee Dee Belemnite (VPDB).

3.6. Gypsum hydration waters

Gypsum samples were ground and dried in a 30 °C oven for 24 h to remove absorbed water and fluid inclusions. Hydration water was extracted using a semi-automated extraction system – the WASP (Water Analyser Sample Preparation) Device developed at the University of Cambridge (Gázquez et al., accepted) (see SI for details). Water oxygen and hydrogen isotopes were measured simultaneously by cavity ringdown laser spectroscopy (CRDS) using a Picarro L1102-i water isotope analyzer and A0211 high-precision vaporizer at the University of Cambridge. Each sample was injected nine times into the vaporizer. Memory effects from previous samples were avoided by rejecting the first three analyses. Values for the final six injections were averaged with in-run precision of less than ±0.1 for $\delta^{18}O$ and ±0.6 for δD (1σ). Calibration of results to V-SMOW was achieved by analyzing internal standards (JRW, ENR, BOTTY, SPIT) before and after each set of 7 or 8 samples. Internal standards were calibrated against V-SMOW, GISP, and SLAP. All results are reported in parts per thousand (‰) relative to V-SMOW. External error, less than ±0.1‰ and ±0.8‰ for $\delta^{18}O$ and δD, respectively, was estimated by repeated analysis of an internal gypsum standard, New-Gyp ($n = 5$).

3.7. Microthermometric analysis

The method for microthermometric analysis closely followed that described by Attia et al. (1995). Thin (<1 mm) samples of gypsum were obtained by cleaving the mineral along 010 planes using a razor blade. The fragments were placed in a Linkam THMSG600 heating-freezing stage attached to a Zeiss Axio Scope.A1 microscope equipped with a 100× objective (see SI for details).

3.8. Scanning electron microscopy (SEM)

SEM analyses of marl samples were performed with a Zeiss Supra 50 VP equipped with an energy dispersive X-ray detector for element analysis (EDX) (see SI for details).

4. Results

4.1. $\delta^{34}S$ and $\delta^{18}O$ of sulfate

Twenty-four samples were analyzed for sulfur isotopes and nineteen samples were analyzed for oxygen isotopes of sulfate (SI Tables 1 and 2). These data are shown in Fig. 3 relative to the expected range of gypsum precipitated from Miocene seawater.

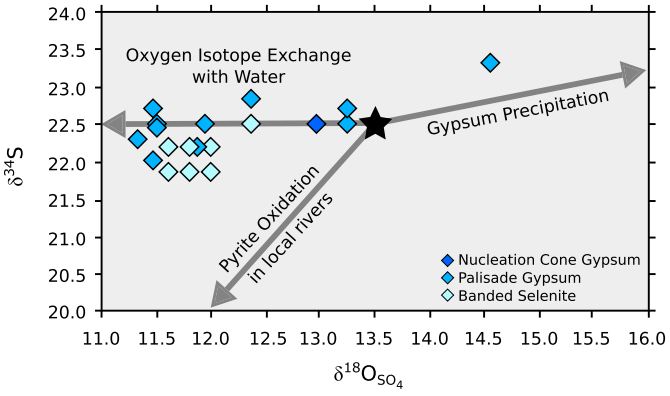

Fig. 3. $\delta^{34}S$ vs. $\delta^{18}O$ of sulfate of the Yesares Gypsum. Messinian seawater values of ~22.5‰ and ~13.5‰ for $\delta^{34}S$ and $\delta^{18}O_{SO_4}$, respectively (Paytan, 1998; Turchyn and Schrag, 2004), are marked with star.

$\delta^{34}S$ varies between 21.9 and 23.3‰ V-CDT and $\delta^{18}O_{SO_4}$ between 11.3 and 14.5‰ V-SMOW. There are negligible differences in the isotope composition among the nucleation cone, palisade, banded selenite, and supercone samples and $\delta^{34}S$ and $\delta^{18}O_{SO_4}$ display no systematic changes with depth in the section.

4.2. Sr isotopes

Six samples from Cycle 6 were measured for strontium isotopic analysis (SI Table 1). The range of $^{87}Sr/^{86}Sr$ is small (29 ppm), varying between 0.708942 and 0.708971. These values falls slightly below the range of strontium isotope seawater expected for the Messinian (McArthur et al., 2001) (Fig. 4).

4.3. XRD, weight %calcite and weight %dolomite of bulk carbonates

Thirty-one marl samples were analyzed by XRD (SI Table 3). The results are semi-quantitative and indicative of the relative abundances of common mineralogical components only. In addition to clay, the major phases are gypsum, calcite, and dolomite and each occurs in varying proportions in Cycle 6. The marls at the base of the section contain both calcite and dolomite. The ratio of calcite to dolomite in the lower marls decreases up-section such that dolomite becomes more dominant toward the gypsum–marl contact (Fig. 5A). Fine-grained gypsum within the marl is abundant in the upper marl from 8 cm below the marl–gypsum contact. Marls juxtaposed to supercones are purely dolomitic and contain varying proportions of gypsum.

4.4. $\delta^{18}O_{carb}$ and $\delta^{13}C$ of bulk carbonates

The oxygen and carbon isotope composition of thirty-seven carbonate samples vary widely from −3.7 to 3.5‰ for $\delta^{18}O_{carb}$ and from −4.9 to 1.5‰ for $\delta^{13}C$ (SI Table 4; Fig. 6). The carbon and oxygen isotope composition of the carbonates are within the range of other Messinian carbonates associated with evaporites in the Mediterranean (Longinelli, 1979). Marls at the base of Cycle 6 ranged from −3.7 to 1.9‰ for $\delta^{18}O_{carb}$ and between −0.1 and 1.5‰ for $\delta^{13}C$. In contrast, marls juxtaposed with the supercones show relatively high $\delta^{18}O_{carb}$ ($2.8 < \delta^{18}O_{carb} < 3.5$‰) and low $\delta^{13}C$ values ($-4.9 < \delta^{13}C < -3.8$‰).

4.5. Gypsum hydration waters

Forty-seven samples representing massive, banded and branching selenite were analyzed for their gypsum hydration water (SI Tables 1 and 2). The measured $\delta^{18}O$ of gypsum hydration water ranges from 1.4‰ to 7.8‰ and δD from −35.9‰ to −2.0‰. Five

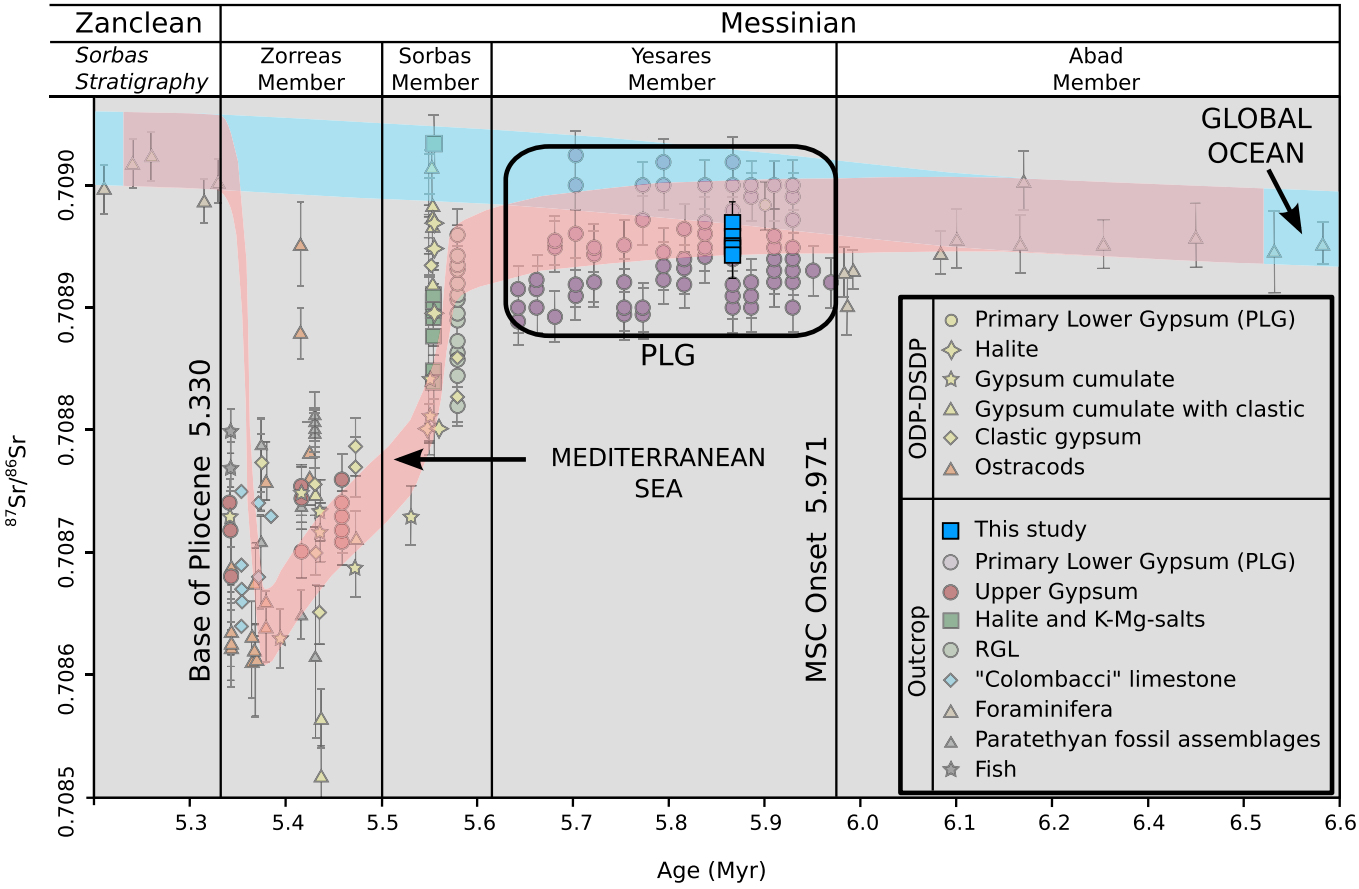

Fig. 4. Sr isotope curve during the Messinian in the Mediterranean Sea and Global Ocean. The progressive change in the isotopic composition of Mediterranean waters during the MSC occurred because of the restricted exchange with the global ocean due to closure of the gateways as well as a contribution of freshwater with low $^{87}Sr/^{86}Sr$ from rivers (e.g. Nile and Rhone) or from the Paratethys (Roveri et al., 2014b). $^{87}Sr/^{86}Sr$ data from this study are plotted at 5.867 Ma in accordance with the cyclostratigraphic dating of cycle 6 (Krijgsman et al., 2001). Sorbas Basin stratigraphy after Krijgsman et al. (2001). Figure modified after Roveri et al. (2014b).

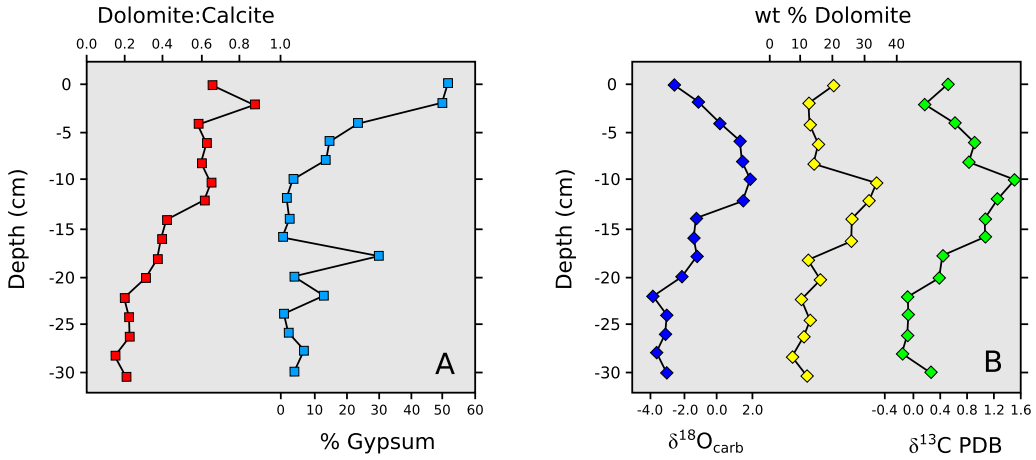

Fig. 5. (**A**) The ratio of dolomite to calcite of the marls at the base of the section. % gypsum is obtained from XRD data; (**B**) $\delta^{18}O_{carb}$, $\delta^{13}C$ and % dolomite in the marls at the base of the section. 0 cm is the gypsum–marl contact.

modern gypsum samples were also analyzed from the Salina at Cabo de Gata, Almería, Spain. The $\delta^{18}O$ of gypsum hydration water ranged from 10.3‰ to 11.6‰ and the δD from 9.6‰ to 18.62‰. The oxygen and hydrogen isotope composition of the parent water in which the gypsum formed is calculated by correcting for the fractionation factors (α):

$$\alpha = \frac{(1000 + \delta^{18}O_{SMOW})}{(1000 + \delta^{18}O_{Brine})}$$

Fractionation factors were assumed to be 1.004 and 0.98 for oxygen and hydrogen isotopes, respectively (Gonfiantini and Fontes, 1963; Fontes and Gonfiantini, 1967; Hodell et al., 2012). Following correction, the $\delta^{18}O$ of the gypsum mother water for Messinian samples is estimated to have ranged between −2.6‰ and 3.8‰ and the δD from −16.2‰ to 18.4‰. The $\delta^{18}O$ of the gypsum mother water of modern Salina samples ranged between 6.2‰ and 7.6‰ and the δD from 30.2‰ to 39.4‰ (Fig. 7).

The $\delta^{18}O$ and δD of gypsum mother water show a systematic change through Cycle 6 (Fig. 8). The most negative $\delta^{18}O$ and δD values are found at the base of the section in the nucleation cone, which represents the first gypsum to precipitate above the marl. $\delta^{18}O$ and δD increase up section into the gypsum palisade reaching maximum values of 3.8‰ and 18.4‰, respectively, at 56 cm. Above this peak, $\delta^{18}O$ and δD fall to average values of −0.2‰ and −2.5‰, respectively, in the banded selenite above 130 cm. Isotope values in the supercones are lower than those below with average values of −0.4‰ for $\delta^{18}O$ and −4.7‰ for δD. The top of the supercone has the lowest $\delta^{18}O$ and δD values of −1.4‰ and −12.1‰, respectively. Thus, the entire section displays a systematic change from low isotopic values at the base (nucleation cone), to maximum values in the middle (palisade gypsum), and a return to low isotopic values near the top (supercone).

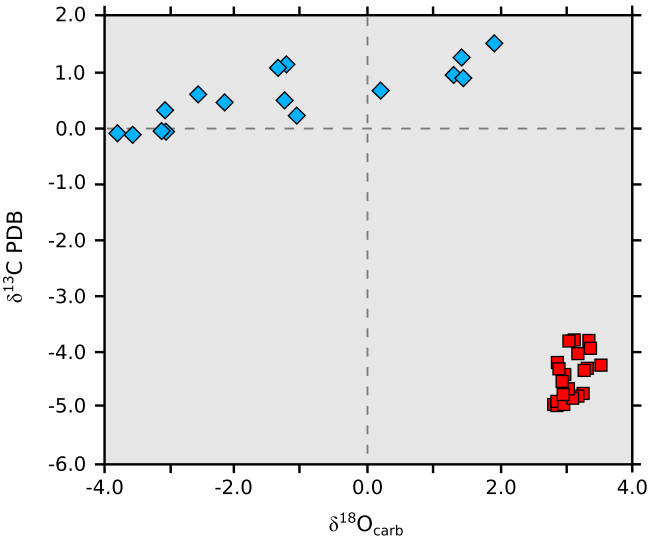

Fig. 6. $\delta^{18}O$ and $\delta^{13}C$ of carbonates from the marl intervals within the Yesares Formation. Diamonds are marls taken from the base of Cycle 6; squares are marls taken from beds juxtaposed to supercones.

4.6. Microthermometric analysis

Eleven samples from the Messinian gypsum of the Sorbas Basin and two samples from the modern Salina at Cabo de Gata, Almería, Spain, were selected for microthermometric analysis (SI Table 5). Primary inclusions in Messinian gypsum froze at temperatures between −40 and −60 °C, with simultaneous shrinkage of the vapor bubble. During heating, first melting was observed between −42 and −32 °C, but this transition is easily missed.

The final melting temperature (Tm_{ice}) for massive, banded and branching selenite is recorded in SI Table 5 and SI Fig. 3. The Tm_{ice} of 101 primary Messinian inclusions ranged between −0.2 °C and −5.2 °C. The average Tm_{ice} was −1.68 °C. Using the revised equation and table for determining the freezing point depression of H_2O–NaCl solutions of Bodnar (1993), salinities estimates range from 0.35% to 8.14% (average 2.85 wt% NaCl equivalent). Tm_{ice} of modern gypsum from the Cabo de Gata Salina ranged between −8.0 and −10.1 °C (average −8.8 °C), corresponding to an average salinity of 12.6%.

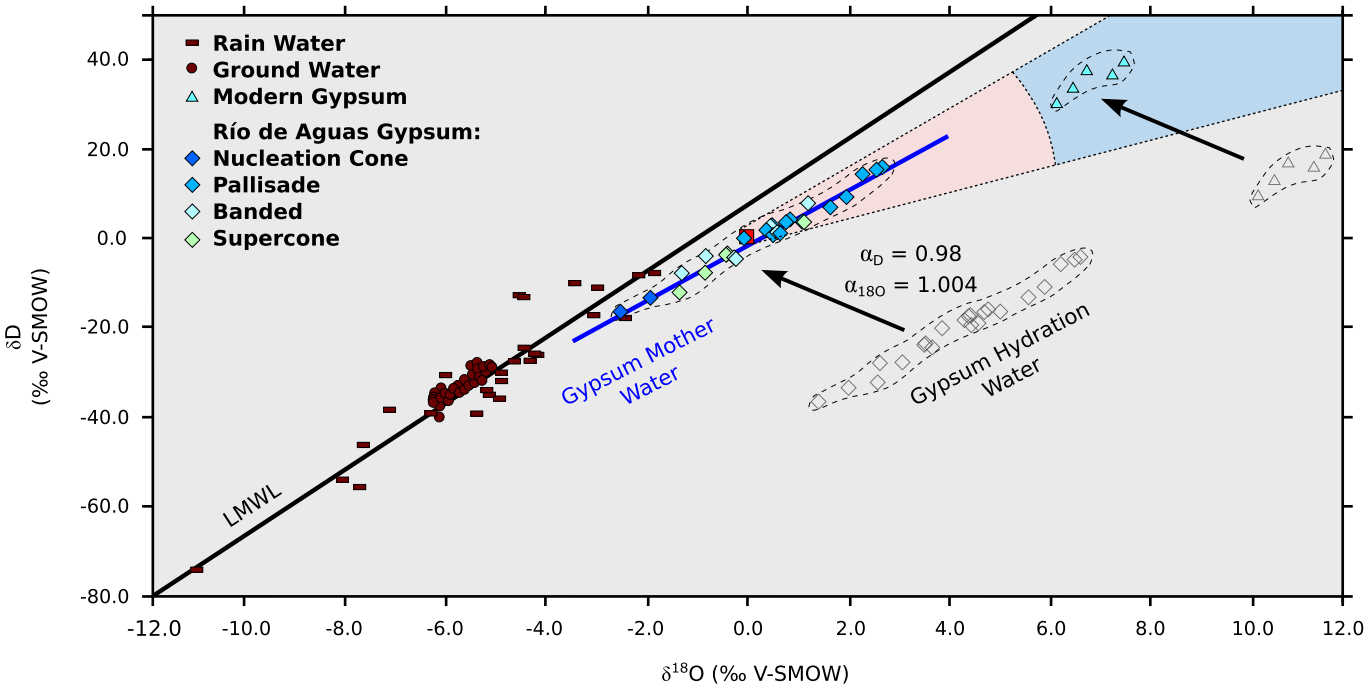

Fig. 7. Diagram of $\delta^{18}O$ vs. δD. $\delta^{18}O$ and δD of rain water (dashes), surface and ground water (circles), gypsum hydration water as measured from Yesares gypsum (open diamonds), and predicted Messinian brine mother water values for the differing facies of Cycle 6 of the Yesares gypsum after correction for fractionation factors (colored diamonds). Grey dashed lines encompass gypsum hydration water and gypsum mother water; the solid black line represents the local meteoric water line (LMWL) estimated by regression through rain, surface and groundwater data ($\delta D = 7.30 \cdot \delta^{18}O + 7.75$; $r^2 = 0.8838$); the blue line represents the evaporative line estimated by least-squares linear regression using mother-water data of Messinian gypsum ($\delta D = 6.06 \cdot \delta^{18}O - 1.27$; $r^2 = 0.9760$). Light blue triangles are modern gypsum data from the Cabo de Gata Salina. Red square is Standard Mean Ocean Water (SMOW). The trajectories for the evaporation of seawater (with starting composition SMOW) for high (slope 7) and low (slope 2.5) humidities are shown, defining a range of possible $\delta^{18}O$ and δD values (pink field). Gypsum precipitation takes place at 3 to 7 times concentrated seawater; gypsum saturation (blue field) is calculated using the Rayleigh Distillation equation, assuming initial $\delta^{18}O$ and δD values of 0‰, and gypsum saturation occurring at an evaporation ratio of 3.8× (evaporation ratio = weight of H_2O of original seawater divided by weight of H_2O in residual evaporated brine). Errors are less than the width of the symbols. (For interpretation of the references to color in this figure legend, the reader is referred to the web version of this article.)

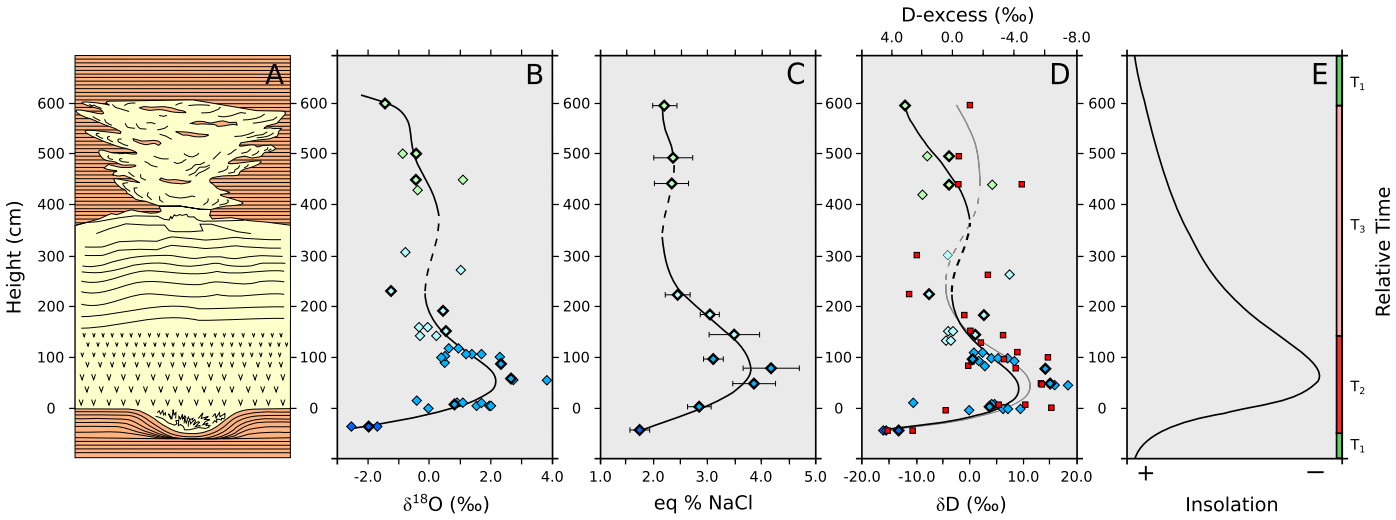

Fig. 8. (**A**) Schematic diagram of Cycle 6 scaled to height of the section, showing carbonate marls at the base and top, a nucleation cone at the base of the gypsum, gypsum palisade, banded selenite and supercone. Data points in **B**, **C** and **D** are plotted relative to the height from which the samples were taken. Samples used for both $\delta^{18}O/\delta D$ and fluid inclusion salinity measurements are highlighted with a bold outline. (**B**) $\delta^{18}O$ (V-SMOW) of gypsum mother water vs. height in section; 1-standard deviation is the width of the symbol. (**C**) Eq% NaCl vs. height in section. Eq% NaCl calculated from the final melting temperatures of ice using the equation of Bodnar (1993). Error bars denote one standard error. (**D**) δD (diamonds, black trend line) of gypsum mother water and d-excess (squares, gray trend line) vs. height in section. d-excess $= \delta D - 8 \cdot \delta^{18}O$ (Craig, 1961); note that the d-excess axis is reversed. 1-standard deviation is the width of the symbol. All trend lines are 5th Order Polynomial Regressions. (**E**) Hypothetical insolation curve, where T_1 denotes the humid period during marl deposition, T_2 denotes the period of gypsum palisade formation at the peak of the cycle, and T_3 denotes the time period during banded selenite and supercone growth; $T_1 + T_2 + T_3$ is equal to approximately 21 ka, although the relative duration of T_1, T_2 and T_3 is unknown.

The Tm_{ice} of fluid inclusions show a systematic change during Cycle 6. When Tm_{ice} values are converted to wt% NaCl equivalent, the curve co-varies with the $\delta^{18}O$ and δD of gypsum hydration water data (Fig. 8). Nucleation cone samples at the base of the section display the highest melting temperatures (averaging a Tm_{ice} of $-1.0\,^{\circ}C$) and lowest salinities. Moving up into the palisade gypsum, the lowest Tm_{ice} and greatest salinity values occur at 87 cm, averaging $-2.55\,^{\circ}C$ and 4.2 wt% NaCl equivalent, respectively. Above this maximum, values increase throughout the banded selenite, from average Tm_{ice} values of $-2.10\,^{\circ}C$ at the base to $-1.44\,^{\circ}C$ at 231 cm. Supercone Tm_{ice} values are more positive again, but collectively are very similar, averaging a Tm_{ice} of $-1.39\,^{\circ}C$.

5. Discussion

An outstanding question regarding the depositional environment of Messinian gypsum in marginal basins of the Mediterranean is whether the gypsum was precipitated directly from seawater or was influenced by meteoric water (e.g. Longinelli, 1979; Müller and Mueller, 1991; Attia et al., 1995; Playà et al., 2000; Flecker et al., 2002; Lu and Meyers, 2003; Lugli et al., 2010; Natalicchio et al., 2014). Strontium and sulfur isotope results favor a dominantly marine origin whereas hydration water and fluid inclusion data support a significant contribution by meteoric water. Below we discuss these seemingly contradictory interpretations and propose an explanation to reconcile the geochemical data.

5.1. Strontium, sulfur and oxygen isotopes of gypsum

Our measured $\delta^{34}S$ of gypsum in Cycle 6 of the Sorbas Basin ranges between 21.9‰ and 23.3‰ CDT (Fig. 3), which agrees with those measured in other Messinian evaporite deposits (e.g. Longinelli, 1979; Lu and Meyers, 2003; Lugli et al., 2007), and is similar to Miocene seawater as reconstructed through pelagic marine barite from the equatorial Pacific ($\sim 22.5 \pm 0.5$‰ CDT; Paytan, 1998). This suggests that the Mediterranean Sea in the Miocene was connected to and isotopically similar to the global ocean. Similarly, the measured $\delta^{18}O_{SO_4}$ of Yesares gypsum (11.3‰ to 14.5‰) is similar to the $\delta^{18}O_{SO_4}$ of Miocene seawater sulfate, reconstructed from pelagic marine barite ($\sim$13.5‰; Turchyn and Schrag, 2004). The fact that seawater values are measured for sulfur and sulfate–oxygen isotopes in the gypsum of the Yesares Member suggest that deposition was dominantly in a marine environment (e.g. Müller and Mueller, 1991; Lu and Meyers, 2003).

It has been suggested that gypsum precipitates with a negligible sulfur isotope fractionation, but as much as a 3‰ offset for oxygen isotopes (Fig. 3) (Lloyd, 1968). However, this oxygen isotope fractionation factor remains poorly constrained, and the isotope composition of a multiply evaporated basin may evolve over time. If the sulfate from Miocene seawater trapped in the Mediterranean were quantitatively precipitated, then, by mass conservation, the $\delta^{34}S$ and $\delta^{18}O_{SO_4}$ of the bulk precipitated gypsum should reflect Miocene seawater. Subsequent solution–reprecipitation of the gypsum in water with a similar $\delta^{34}S$ or $\delta^{18}O_{SO_4}$ will not alter the $\delta^{34}S$ or $\delta^{18}O_{SO_4}$ of the gypsum significantly. Abiotic oxygen isotope exchange between aqueous sulfate and water does not occur over geologically relevant timescales (Lloyd, 1968; Rennie and Turchyn, 2014).

The sulfur and sulfate–oxygen isotope composition of meteoric water that could have been supplied to the site of gypsum formation would largely reflect the isotope composition of sulfur-bearing minerals that are being locally weathered. Measurements of the $\delta^{34}S$ and $\delta^{18}O_{SO_4}$ in Spanish rivers today are heavily biased towards evaporite values (high $\delta^{34}S$ and $\delta^{18}O_{SO_4}$) owing to the ongoing weathering of the Messinian evaporites. However, underneath these evaporites exist sedimentary deposits containing shale beds that plausibly bear pyrite, and it is possible that oxidative pyrite weathering could have dominated the terrestrial sulfate–isotope signal during the MSC. Oxidative weathering of pyrite produces river sulfate that is enriched in the ^{32}S isotope and typically with a $\delta^{18}O_{SO_4}$ similar to the $\delta^{18}O$ of the water (Calmels et al., 2007). If a significant amount of sulfate used to make the Yesares gypsum were derived from terrestrial sources, then we hypothesize the $\delta^{34}S$ and $\delta^{18}O_{SO_4}$ of the gypsum would be significantly lower than what we measure.

$^{87}Sr/^{86}Sr$ of a semi-enclosed marginal basin is similarly a function of the balance between ocean and riverine input, both of which are characterized by different strontium concentrations and

$^{87}Sr/^{86}Sr$. Because of the long residence time of strontium relative to the mixing time of the ocean, $^{87}Sr/^{86}Sr$ is homogeneous in the global ocean. The $^{87}Sr/^{86}Sr$ of Messinian seawater is well established with values varying between 0.70900 and 0.70903 during the MSC (McArthur et al., 2001). There is no fractionation of strontium isotopes during gypsum precipitation; thus, a direct comparison can be made between the $^{87}Sr/^{86}Sr$ of gypsum and the parent solution.

Measured $^{87}Sr/^{86}Sr$ of the gypsum samples in Cycle 6 of the Río de Aguas section vary between 0.708942 and 0.708971. The values fall slightly below the range of the strontium isotope curve for seawater (McArthur et al., 2001), suggesting that continental waters with a lower $^{87}Sr/^{86}Sr$ than contemporaneous Miocene seawater may have modified the brine within the Sorbas Basin. However, the values are within the range given by Roveri et al. (2014b) for Mediterranean $^{87}Sr/^{86}Sr$ seawater values between 5.97 and 5.60 Ma (Fig. 4). While the $^{87}Sr/^{86}Sr$ values of the Río de Aguas do not indicate formation of gypsum from global seawater, they could represent Messinian Mediterranean seawater with little local freshwater input. The $^{87}Sr/^{86}Sr$ data, coupled with $\delta^{34}S$ and $\delta^{18}O_{SO_4}$ data, imply little, if any, contribution of meteoric water to the brine that formed the Yesares Gypsum (Longinelli, 1979; Lugli et al., 2010).

5.2. Gypsum hydration water and microthermometry

The observed range of $\delta^{18}O$ and δD of gypsum mother water ($-2.6‰$ to $3.8‰$ for $\delta^{18}O$ and $-16.2‰$ to $18.4‰$ for δD) is significantly lower than expected from gypsum formed solely from the evaporation of seawater. Assuming a starting point of seawater with modern $\delta^{18}O$ and δD values, Fig. 7 shows the possible trajectories of $\delta^{18}O$ and δD for evaporative concentration under conditions of high and low humidity. Modern gypsum measured from the Salina at Cabo de Gata falls in the region of predicted gypsum saturation for evaporated seawater. If the gypsum precipitated in the Sorbas Basin were solely of marine origin, we would expect the values to fall along a mixing line within this zone of gypsum saturation. Instead all $\delta^{18}O$ and δD values from Cycle 6 fall well below the saturation point for gypsum on the evaporative line. This implies that the Yesares Gypsum was precipitated from a hybrid brine, consisting of a mixture of seawater and meteoric water.

An alternative explanation of the low $\delta^{18}O$ and δD of hydration water is that the values don't reflect the original brine but have undergone postdepositional isotopic exchange of the crystallization water with meteoric water. The kinetics of the isotopic exchange of gypsum hydration water is not well studied, but Sofer (1978) concluded gypsum hydration water only retains its isotopic composition under dry conditions (e.g. Negev Desert) and exchanges isotopically under humid conditions. He suggested the gypsum hydration method can only be applied to primary gypsum that has not undergone dehydration, exchange, or recrystallization, and thus has retained its original water isotopic composition. To test if the isotope composition of gypsum hydration water is reliable in the Sorbas Basin, we directly compared gypsum hydration water isotopic results with microthermometric analysis of primary fluid inclusions from the same samples.

Primary fluid inclusions trap the parent brine and reflect the composition of the solution from which the gypsum precipitated (Attia et al., 1995). Microthermometric data show that no Messinian fluid inclusions have salinities high enough to be within the range of gypsum saturation if evaporated from seawater (SI Table 5). Gypsum first precipitates during the evaporation of seawater at a wt% NaCl equivalent of ~11%, which should correspond to a Tm_{ice} of -7 to $-8\,°C$ (Attia et al., 1995; Natalicchio et al., 2014). In comparison, the fluid inclusions from the modern Salina samples melted at $-8.8\,°C$ corresponding to 12.6 wt% NaCl equivalent, and are above the point of gypsum saturation. In contrast, Messinian fluid inclusions from the Río de Aguas section have wt% NaCl equivalent ranging from 0.4% to 8.1% (averaging 2.9 wt% NaCl equivalent), indicating that the brine from which gypsum formed was dilute relative to seawater (Attia et al., 1995; Natalicchio et al., 2014).

Using the equation of Goldstein and Reynolds (1994), we converted wt% NaCl equivalent to salinity in parts per thousand (ppt) seawater. The salinity of primary Messinian fluid inclusions is highly correlated with $\delta^{18}O$ and δD of gypsum mother water, yielding an r^2 of 0.88 and 0.87, respectively (Fig. 9). The intercepts of the regression equations and salinity are $-4.4 \pm 1.3‰$ for $\delta^{18}O$ and $-28.9 \pm 8.7‰$ for δD. These values define the isotope composition of the freshwater endmember and are within error of the average isotope values of precipitation and groundwater data from the local region of Almería today ($\delta^{18}O = -4.3‰$ and $\delta D = -22.2‰$; IAEA, 2005). These results provide strong evidence that both the fluid inclusion and gypsum hydration water are representative of the mother brines in which the gypsum formed and postdepositional isotopic exchange has not occurred. These results also imply that the mother fluid from which the gypsum was precipitated was influenced by meteoric water.

5.3. Decoupling of the source of ions and water during gypsum formation

An inconsistency exists between the marine origin of gypsum implied by strontium isotopes, sulfur and oxygen isotopes of sulfate and the significant meteoric influence inferred from the $\delta^{18}O$ and δD of gypsum hydration water and the salinities of fluid inclusions. The formation of the Primary Lower Gypsum is most commonly attributed to the evaporation from brines produced by continuous inflow of seawater from the Atlantic Ocean, providing the ion supply necessary for gypsum precipitation, coupled with episodes of reduced outflow under dryer climate conditions (Krijgsman and Meijer, 2008; Topper and Meijer, 2013). A nonmarine origin of Messinian gypsum in marginal basins raises questions concerning the marine signatures of strontium, sulfur, and oxygen isotopes in sulfate and the source of calcium and sulfate ions needed for the formation of such large gypsum deposits. An alternate mechanism is needed to explain the lower salinities inferred from fluid inclusion and isotopic results in the Río de Aguas section.

One interpretation is that strontium isotopes, sulfur and oxygen isotopes in sulfate are relatively insensitive to freshwater inputs and are therefore not recording the dilution of seawater by nonmarine fluids. For example, assuming standard marine and freshwater strontium concentrations and a $^{87}Sr/^{86}Sr$ freshwater endmember value of 0.7090 ± 0.001, >20% freshwater influx would be needed to produce a nonmarine strontium isotope signature in a typical brine (e.g. 4× the concentration of seawater) (Lu and Meyers, 2003; Flecker et al., 2002). Sulfate concentrations in terrestrial waters are even lower, with most rivers containing three orders of magnitude less sulfate than seawater. While this hints that strontium isotopes, sulfur and sulfate–oxygen isotopes are relatively insensitive to freshwater inputs, the volumes of freshwater needed to generate the low salinities inferred from inclusions and hydration water require an evaporated seawater brine to be diluted by over 50% for the majority of samples. This volume of meteoric water input is well above the modeled threshold necessary to observe a nonmarine signature in strontium isotopes, sulfur and sulfate–oxygen isotopes.

A plausible explanation is sulfate and strontium molecules are decoupled from the source of the water for the gypsum hydration water, which was a mixture of marine and terrestrial sources.

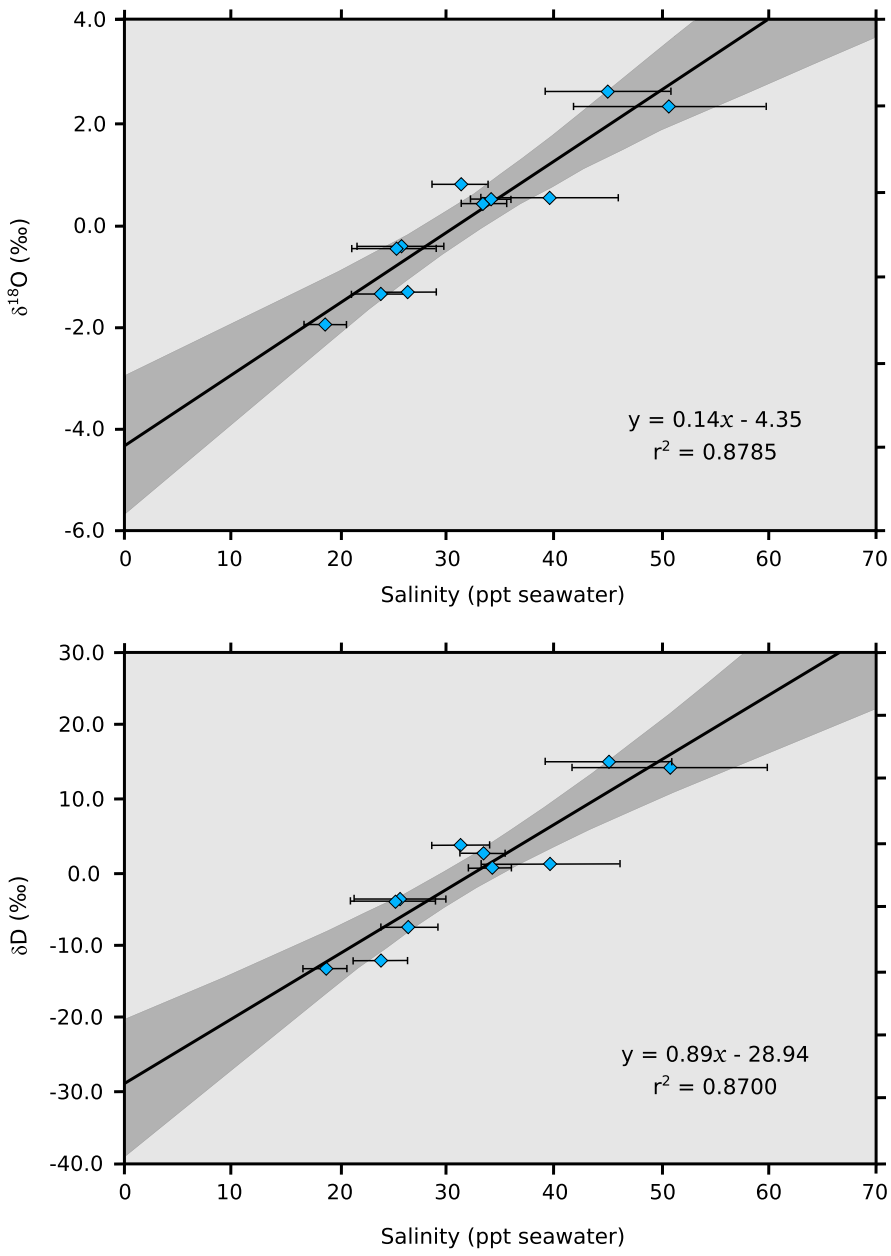

Fig. 9. Coupled measurements of $\delta^{18}O$ and δD of hydration water and salinity of fluid inclusions in Messinian Gypsum. Salinities calculated from the final melting temperatures of ice using the equation of Goldstein and Reynolds (1994). The dark gray band denotes 95% confidence limits. The y intercept at zero salinity defines the freshwater $\delta^{18}O/\delta D$ endmember. Error bars denote 1-standard error. 1-standard deviation in $\delta^{18}O$ and δD is the edge of the symbol.

The source of the sulfate and strontium may come from dissolution of previously deposited marine gypsum that recharged the basin and maintained gypsum saturation. Evaporation of this fluid would produce a brine with the observed $\delta^{18}O$ and δD values and salinities, while retaining marine $^{87}Sr/^{86}Sr$, $\delta^{34}S$ and $\delta^{18}O_{SO_4}$ values because of low concentrations of these elements in meteoric water. This mechanism has been proposed previously by Natalicchio et al. (2014) to explain salinity inferred from fluid inclusions in gypsum from the Piedmont Basin (Italy).

5.4. Deposition of the lower marl unit

The carbonate in the marl at the base of Cycle 6 is a mixture of calcite and dolomite (Fig. 5A; SI Table 4). There is an increase in the proportion of dolomite/calcite towards the top of the marl where it transitions into the gypsum unit above. The proportion of gypsum in the marls increases in the 8 cm below the transition into the massive gypsum above the marl. This progression of calcite to dolomite to gypsum is indicative of fractional crystallization of minerals by evaporative enrichment (Eugster, 1980).

The $\delta^{18}O_{carb}$ and $\delta^{13}C$ values of bulk carbonate in the lower marl unit increase from −3.7‰ and −0.1‰, respectively, at the base to a maximum of 1.9‰ and 1.5‰ at 10 cm below the transition into the massive gypsum before decreasing in the top of the lower marl unit (Fig. 5B). The $\delta^{18}O_{carb}$ and $\delta^{13}C$ of bulk carbonate is expected to be higher in the marls dominated by dolomite because of the different isotope fractionation factor for oxygen and carbon isotopes between calcite and water, and dolomite and water; the oxygen and carbon isotope composition of dolomite is ~2.6‰ and ~2.4‰ greater than calcite when formed in equilibrium (Vasconcelos et al., 2005; Sheppard and Schwarcz, 1970). This indicates that a good correlation exists between the percent dolomite and bulk $\delta^{18}O_{carb}$ and $\delta^{13}C$. The relatively positive $\delta^{13}C$ in the marls at the base of the section suggest there is not signifi-

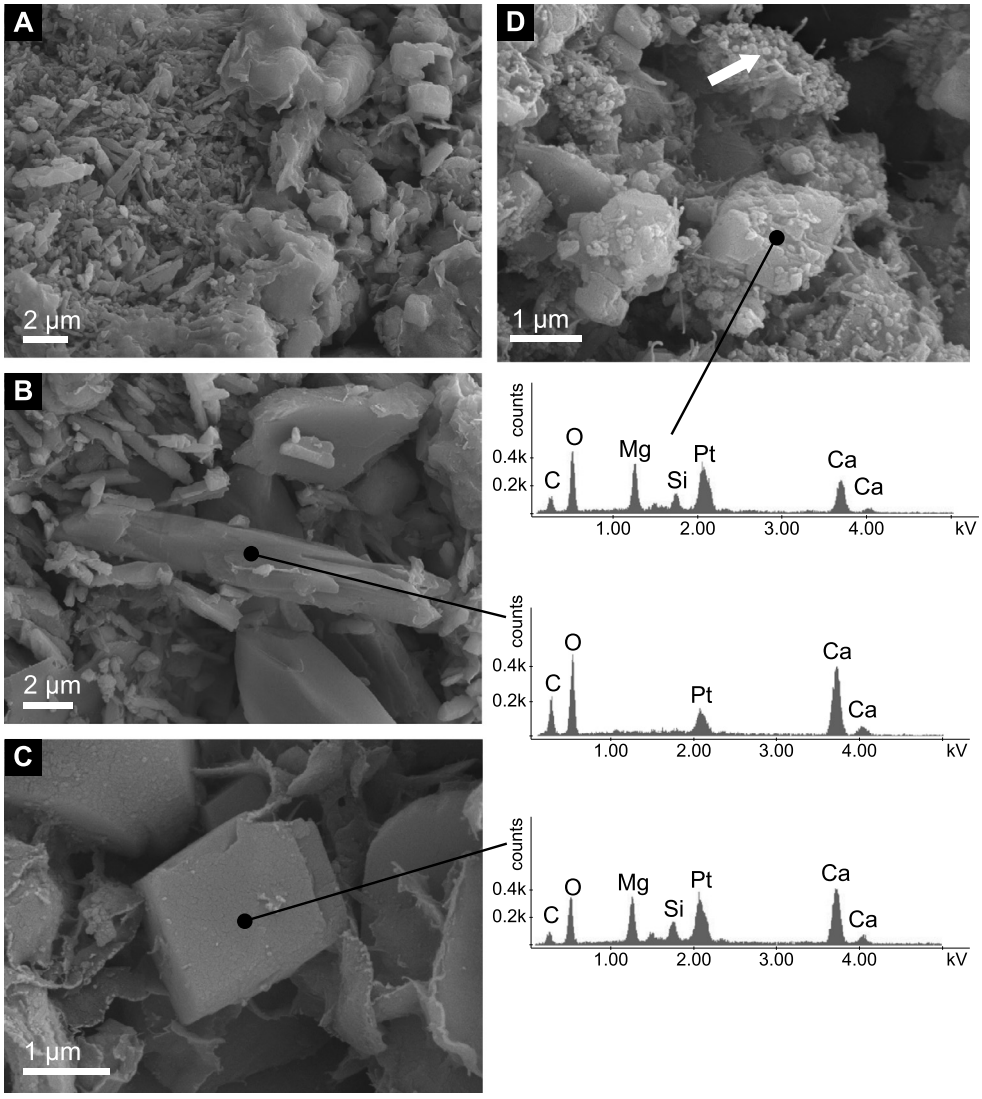

Fig. 10. Scanning electron microscopy (SEM) photomicrographs and energy dispersive X-ray (EDX) analyses of the carbonate minerals present in the studied samples. (**A**) Image of a representative sample of the lower marl unit (i.e., RdA1 −25 cm). Calcite crystals are characterized by an elongated, almost acicular morphology, while dolomite crystals display a rhombohedral habit. No morphological evidence indicates that dolomite formed through a diagenetic replacement of calcite or whether it is a primary precipitate. Both calcite and dolomite are authigenic. (**B**) Typical calcite crystal present in the lower unit and corresponding EDX spectrum, which is consistent with a Ca-carbonate. (**C**) Typical dolomite crystal present in the lower unit and corresponding EDX spectrum, which is consistent with dolomite. (**D**) Image of representative dolomite crystals present in the upper unit (i.e., SC marl 100) and corresponding EDX spectrum. Rhombohedral crystals of dolomite seem to form through aggregation of dolomite nanoglobules (white arrow), which suggests that dolomite in the "supercone unit" is a primary precipitate. Dolomite crystals that form through aggregation of nanoglobules are typically observed in microbially mediated dolomite. Pt peaks in all EDX spectra are due to the metal coating used for sample preparation. Si peaks in the spectra measured from dolomite are interpreted as a contamination from the surrounding authigenic silicate minerals.

cant oxidation of organic carbon, which would drive the $\delta^{13}C$ lower (Fig. 6). SEM investigations show that both calcite and dolomite present in the lower unit are authigenic (Fig. 10). Indeed, no angular or fractured mineral surfaces indicative of transport and mechanical erosion were observed. The elongated, almost acicular, morphology of the calcite crystal as well as the rhombohedral habit of the dolomite is commonly observed in carbonate minerals that form in the peritidal and supratidal zone of modern evaporitic environments (Bontognali et al., 2010). We found no clear morphological evidence (i.e., dissolution/re-crystallization structures, hybrid mineral shapes) suggesting that the dolomite formed through a penecontemporaneous replacement of calcite. Therefore, the progressive enrichment in dolomite vs calcite observed in the studied sequence (Fig. 5A) may have been caused by an environmental change from fresher peritidal marine-waters to more evaporated intertidal/supratidal conditions.

5.5. Formation of the supercone–marl unit

The origin of the supercone structures and associated laminated marls in the Río de Aguas section have prompted much speculation since their initial description by Dronkert (1977; 1985). We have identified important differences in the mineralogical and isotopic composition of the marl at the base of the cycle and the marl associated with the supercones near the top. The carbonate in the marl of the supercone unit is entirely dolomite and display higher $\delta^{18}O_{carb}$ and lower $\delta^{13}C$ values than those in the lower marl unit (Fig. 6).

The supercone selenite and the associated marl are considered to be syndepositional as individual lamina thin and disappear into gypsum crystals. Some laminae wrap around the supercone branches and can be traced above and below. The syndepositional nature of the dolomitic marl and gypsum permits paleotemperature to be estimated if the gypsum and dolomite were formed in

isotopic equilibrium with the same water. The $\delta^{18}O$ of the gypsum hydration water provides the $\delta^{18}O$ of the water whereas the $\delta^{18}O_{carb}$ of the dolomite provides the carbonate value (Hodell et al., 2012). Marl sample SC50-10 ($\delta^{18}O_{dolomite} = 3.05‰$) is directly juxtaposed to gypsum sample SC50B ($\delta^{18}O = 1.08‰$), and together yield a temperature of 19.2 °C using the dolomite–water paleotemperature equation of Vasconcelos et al. (2005). This temperature is close to the average sea surface temperature from the local region of Almería today (15–25 °C). It also agrees with Messinian sea surface temperatures (17–18 °C) obtained from fluid inclusion analyses in Messinian halite (Speranza et al., 2013). These reasonable temperature estimates provide support that the dolomite and gypsum of the marl–supercone beds were formed at the same time from water with similar $\delta^{18}O$ values.

The marls associated with the supercones are very finely laminated and lack any evidence of bioturbation indicating anoxic conditions, and are reminiscent of the anoxic dolomite found in the Messinian Tripoli Formation in the deep basin (McKenzie et al., 1979). The $\delta^{13}C$ of the dolomite is low and varies between −3.8 and −4.9‰, indicating a source of dissolved inorganic carbon at least partially derived from the oxidation of organic matter; thus, the formation of the dolomite may be microbially mediated (Vasconcelos et al., 1995; Vasconcelos and McKenzie, 1997). This interpretation is also supported by the morphology of the dolomite crystals, which form through aggregation of spherical/amorphous nanoglobules (Fig. 10D). In a study conducted with sulfate reducing bacteria capable of mediating dolomite formation, Bontognali et al. (2008) demonstrate that such nanoglobules represent the early stage of mineral nucleation within microbially produced extracellular polymeric substances (EPS). Nanoglobules that merge to form rhombohedral dolomite have also been observed in microbial mats that occur in the intertidal and supratidal zone of the sabkha of Abu Dhabi (Bontognali et al., 2010). In this modern evaporitic environment, dolomite can co-occur with gypsum crystals. As the sediment ages, only the dolomite (and not the microbial mat) is preserved, similar to observations in the marls juxtaposed to supercones.

5.6. Climate control of gypsum–marl deposition

The gypsum–marl cycles of the Lower Primary Gypsum are purported to represent climatic changes paced by precession with gypsum deposited during more arid conditions and sapropelic marl during more humid conditions (Krijgsman et al., 1999, 2001; Krijgsman and Meijer, 2008). The mineralogical and isotopic trends support this interpretation for Cycle 6:

1. The peak wet conditions occurred at the precession minimum (maximum summer insolation) and is represented by the deposition of the laminated marl at the base of the studied section. Climate conditions became progressively drier promoting the formation of dolomite, and finally gypsum towards the top of the lower marl unit (Fig. 5A).
2. As climate became progressively drier, detrital input declined and pure gypsum began to precipitate in nucleation cones. The hydration water of the gypsum in the nucleation cones has relatively low $\delta^{18}O$ and δD and the fluid inclusions indicate relatively low salinity compared to the gypsum above (Fig. 8).
3. Salinity, $\delta^{18}O$ and δD progressively increased above the nucleation cones reaching a maximum in the massive selenite palisade unit, marking peak aridity associated with the precession maxima (summer insolation minimum). A highly stratified brine, which in relation to total water depth produces a high and stable pycnocline (the gypsum saturation interface), creates the condition necessary for massive selenite growth (Bąbel, 2007). The $\delta^{18}O$ and δD and salinity of the palisade gypsum support formation at a low saturation state needed for slow crystal growth (Bąbel, 2007).
4. After formation of the gypsum palisade, the trend in aridity reversed indicating a progressive decrease in salinity related to increased freshwater input as recorded by decreasing salinity, $\delta^{18}O$ and δD values of the banded selenite unit.
5. As precipitation increased with falling summer insolation, the supercones and associated dolomitic marls began to be deposited. The salinity of fluid inclusions and $\delta^{18}O$ and δD of gypsum in the supercones are lower than the banded and massive selenite units below. Detrital input also increased and led to the deposition of the dolomitic marls juxtaposed to the supercones (Section 5.5). Above the supercone the basal clay unit of Cycle 7 was deposited, marking the return of wetter climate conditions associated with the precession minimum.

6. Conclusions

We made tandem measurements of the isotopic composition of gypsum hydration water and the salinity of fluid inclusions to test whether Messinian gypsum retained the original isotopic composition and salinity of the mother water. After correction of oxygen and hydrogen isotopes of gypsum hydration water for known fractionation factors, we show that the $\delta^{18}O$ and δD of the mother water is highly correlated with salinity of fluid inclusions in gypsum deposits of Cycle 6 within the Yesares Member. The intercepts of the regression equations (i.e., at zero salinity) define the isotope composition of the freshwater endmember. These values are within error of the average isotope composition of precipitation and groundwater data from the local region of Almería today. This agreement provides strong evidence that the gypsum hydration water has retained its isotope composition and has not undergone postdepositional exchange.

The isotope and salinity values indicate a significant contribution of meteoric water during formation of Messinian gypsum in the Sorbas Basin. This observation contrasts with sulfur and oxygen isotopes in sulfate ($21.9 < \delta^{34}S < 23.3‰$; $11.3 < \delta^{18}O_{SO_4} < 14.5‰$) and strontium isotopes ($0.708942 < {}^{87}Sr/{}^{86}Sr < 0.708971$) that are similar to those measured in other Messinian evaporites of the Mediterranean. We suggest the source of the ions for gypsum formation is recycled from previously deposited units, whereas the source of the water is a mixture of marine and meteoric sources. The ${}^{87}Sr/{}^{86}Sr$, $\delta^{34}S$, and $\delta^{18}O_{SO_4}$ retain the signature of the parent sulfate deposits because of low concentrations of these elements in meteoric water, whereas the $\delta^{18}O$ and δD and salinity reflect a mixed signal of marine and freshwater. The recycling of solutes explains the discrepancies between strontium, sulfur and water isotopes by decoupling the geochemical signatures of the ions and water during gypsum formation.

Lastly, we demonstrate that the patterns displayed by the $\delta^{18}O$ and δD and salinity of the gypsum, together with the overall changes in mineralogy (calcite–dolomite–gypsum) in Cycle 6, are consistent with a precession-driven change in climate. Additional studies are needed to determine whether the patterns observed here for Cycle 6 apply to other cycles in the Yesares Member.

Acknowledgements

We thank Ian Mather, James Rolfe and Jason Curtis for laboratory support and technical assistance with stable isotope measurements, Dr Giulio Lampronti for support with the X-Ray Diffractometry measurements and Marie Edmonds and David Neave for use of the Linkam THMSG600 cryostage and associated training. The authors are grateful to Mr. Vicente Suarez and Mr. Francisco Márquez (Grupo Salinas Company) for providing access to the Cabo

de Gata Salinas and to Carmen Guirado, who carried out the sampling. Financial support was provided by Clare College Geological Research Fund to N.P. Evans. The research leading to these results has received funding from the European Research Council under the European Union's Seventh Framework Programme (FP/2007–2013)/ERC Grant Agreement n. 339694 (Water Isotopes of Hydrated Minerals) to D.A. Hodell. We thank two anonymous reviewers for insightful comments that improved the paper.

Appendix A. Supplementary material

Supplementary material related to this article can be found online at http://dx.doi.org/10.1016/j.epsl.2015.07.071.

References

Attia, O.E., Lowenstein, T.K., Wali, A.M.A., 1995. Middle Miocene gypsum, gulf of suez: marine or nonmarine? J. Sediment. Res. 65A (4), 614–626.

Bąbel, M., 2004. Models for evaporite, selenite and gypsum microbialite deposition in ancient saline basins. Acta Geol. Pol. 54 (2), 313–337.

Bąbel, M., 2007. Depositional environments of a salina-type evaporite basin recorded in the Badenian gypsum facies in the northern Carpathian Foredeep. Geol. Soc. (Lond.) Spec. Publ. 285 (1), 107–142.

Bodnar, R., 1993. Revised equation and table for determining the freezing point depression of H_2O–Nacl solutions. Geochim. Cosmochim. Acta 57 (3), 683–684.

Bontognali, T., Vasconcelos, C., Warthmann, R., Bernasconi, S., Dupraz, C., Strohmenger, C., McKenzie, J.A., 2010. Dolomite formation within microbial mats in the coastal sabkha of Abu Dhabi (United Arab Emirates). Sedimentology 57, 824–844.

Bontognali, T., Vasconcelos, C., Warthmann, R., Dupraz, C., Bernasconi, S., McKenzie, J.A., 2008. Microbes produce nanobacteria-like structures, avoiding cell entombment. Geology 36, 663–666.

Calmels, D., Gaillardet, J., Brenot, A., France-Lanord, C., 2007. Sustained sulfide oxidation by physical erosion processes in the Mackenzie River Basin: climatic perspectives. Geology 35 (11), 1003–1006.

Craig, H., 1961. Isotopic variations in meteoric waters. Science (New York, NY) 133, 1702–1703.

Dronkert, H., 1977. The evaporites of the Sorbas basin. Inst. Invest. Geol. Diput. Prov. Univ. Barcelona 32, 55–76.

Dronkert, H., 1985. Evaporite models and sedimentology of Messinian and recent evaporites. GUA Pap. Geol. Ser. 1 (24), 283.

Engleman, E.E., Jackson, L.L., Norton, D.R., 1985. Determination of carbonate carbon in geological materials by coulometric titration. Chem. Geol. 53, 125–128.

Eugster, H.P., 1980. Geochemistry of evaporitic lacustrine deposits. Annu. Rev. Earth Planet. Sci. 8, 35–63.

Flecker, R., De Villiers, S., Ellam, R.M., 2002. Modelling the effect of evaporation on the salinity-$^{87}Sr/^{86}Sr$ relationship in modern and ancient marginal-marine systems: the Mediterranean Messinian Salinity Crisis. Earth Planet. Sci. Lett. 203, 221–233.

Fontes, J., Gonfiantini, R., 1967. Fractionnment isotopique de l'hydrogene dans l'eau de crystallization du gypse. C.R. Acad. Sci. Paris 265, 4–6.

Gázquez, F., Mather, I., Rolfe, J., Evans, N.P., Herwartz, D., Staubwasser, M., Hodell, D.A., accepted. Simultaneous analysis of $^{17}O/^{16}O$, $^{18}O/^{16}O$ and H^2/H^1 of gypsum hydration water by cavity ringdown laser spectroscopy. Rapid Commun. Mass Spectrom.

Goldstein, R.H., Reynolds, T.J., 1994. Systematics of fluid inclusions in diagenetic minerals. In: SEPM Short Course, vol. 31. Society for Sedimentary Geology, p. 199.

Gonfiantini, R., Fontes, J.C., 1963. Oxygen isotopic fractionation in the water of crystallization of gypsum. Nature 200, 644–646.

Hodell, D.A., Turchyn, A.V., Wiseman, C.J., Escobar, J., Curtis, J.H., Brenner, M., Gilli, A., Mueller, A.D., Anselmetti, F., Ariztegui, D., Brown, E.T., 2012. Late glacial temperature and precipitation changes in the lowland Neotropics by tandem measurement of $\delta^{18}O$ in biogenic carbonate and gypsum hydration water. Geochim. Cosmochim. Acta 77, 352–368.

IAEA, 2005. Isotopic composition of precipitation in the Mediterranean Basin in relation to air circulation patterns and climate. Tech. Rep. October, Isotope Hydrology Section International Atomic Energy Agency.

Krijgsman, W., Fortuin, A.R., Hilgen, F.J., Sierro, F.J., 2001. Astrochronology for the Messinian Sorbas basin (SE Spain) and orbital (precessional) forcing for evaporite cyclicity. Sediment. Geol. 140 (1–2), 43–60.

Krijgsman, W., Hilgen, F.J., Raffi, I., Sierro, F.J., Wilson, D.S., 1999. Chronology, causes and progression of the Messinian salinity crisis. Nature 400, 652–655.

Krijgsman, W., Meijer, P.T., 2008. Depositional environments of the Mediterranean "Lower Evaporites" of the Messinian salinity crisis: constraints from quantitative analyses. Mar. Geol. 253 (3–4), 73–81.

Lloyd, R.M., 1968. Oxygen isotope behavior in the sulfate-water system. J. Geophys. Res. 73, 6099.

Longinelli, A., 1979. Isotope geochemistry of some Messinian evaporates: paleoenvironmental implications. Palaeogeogr. Palaeoclimatol. Palaeoecol. 29, 95–123.

Lu, F.H., Meyers, W.J., 2003. Sr, S, and $\{OSO_4\}$ isotopes and the depositional environments of the upper Miocene evaporites, Spain. J. Sediment. Res. 73, 444–450.

Lugli, S., Bassetti, M.A., Manzi, V., Barbieri, M., Longinelli, A., Roveri, M., 2007. The Messinian 'Vena del Gesso' evaporites revisited: characterization of isotopic composition and organic matter. Geol. Soc. (Lond.) Spec. Publ. 285 (1), 179–190.

Lugli, S., Manzi, V., Roveri, M., Schreiber, B.C., 2010. The Primary Lower Gypsum in the Mediterranean: a new facies interpretation for the first stage of the Messinian salinity crisis. Palaeogeogr. Palaeoclimatol. Palaeoecol. 297 (1), 83–99.

Manzi, V., Gennari, R., Hilgen, F., Krijgsman, W., Lugli, S., Roveri, M., Sierro, F.J., 2013. Age refinement of the Messinian salinity crisis onset in the 22 Mediterranean. Terra Nova 25 (4), 315–322.

Manzi, V., Gennari, R., Lugli, S., Roveri, M., Scafetta, N., Schreiber, B.C., 2012. High-frequency cyclicity in the Mediterranean Messinian evaporites: evidence for Solar-Lunar climate forcing. J. Sediment. Res. 82 (12), 991–1005.

Manzi, V., Lugli, S., Roveri, M., Charlotte Schreiber, B., 2009. A new facies model for the Upper Gypsum of Sicily (Italy): chronological and palaeoenvironmental constraints for the Messinian salinity crisis in the Mediterranean. Sedimentology 56, 1937–1960.

McArthur, J., Howarth, R., Bailey, T., 2001. Strontium isotope stratigraphy: LOWESS version 3: best fit to the marine Sr-isotope curve for 0–509 Ma and accompanying look-up table for deriving numerical age. J. Geol. 109 (2), 155–170.

McKenzie, J., Jenkyns, H., Bennet, G., 1979. Stable isotope study of the cyclic diatomite—claystones from the Tripoli formation, Sicily: a prelude to the Messenian salinity crisis. Palaeogeogr. Palaeoclimatol. Palaeoecol. 29 (143), 125–141.

Müller, D.W., Mueller, P.A., 1991. Origin and age of the Mediterranean Messinian evaporites: implications from Sr isotopes. Earth Planet. Sci. Lett. 107, 1–12.

Natalicchio, M., Dela Pierre, F., Lugli, S., Lowenstein, T.K., Feiner, S.J., Ferrando, S., Manzi, V., Roveri, M., Clari, P., 2014. Did late Miocene (Messinian) gypsum precipitate from evaporated marine brines? Insights from the Piedmont basin (Italy). Geology 42 (3), 179–182.

Paytan, A., 1998. Sulfur isotopic composition of cenozoic seawater sulfate. Science 282, 1459–1462.

Playà, E., Ortí, F., Rosell, L., 2000. Marine to non-marine sedimentation in the upper Miocene evaporites of the Eastern Betics, SE Spain: sedimentological and geochemical evidence. Sediment. Geol. 133, 135–166.

Rennie, V.C.F., Turchyn, A.V., 2014. Controls on the abiotic exchange between aqueous sulfate and water under laboratory conditions. Limnol. Oceanogr., Methods 12 (4), 166–173.

Rouchy, J.M., Caruso, A., 2006. The Messinian salinity crisis in the Mediterranean basin: a reassessment of the data and an integrated scenario. Sediment. Geol. 188–189, 35–67.

Roveri, M., Gennari, R., Lugli, S., Manzi, V., 2009. The Terminal Carbonate Complex: the record of sea-level changes during the Messinian salinity crisis. GeoActa 8, 63–77.

Roveri, M., Flecker, R., Krijgsman, W., Lofi, J., Lugli, S., Manzi, V., Sierro, F.J., Bertini, A., Camerlenghi, A., De Lange, G., Govers, R., Hilgen, F.J., Hübscher, C., Meijer, P.T., Stoica, M., 2014a. The Messinian Salinity Crisis: past and future of a great challenge for marine sciences. Mar. Geol. 352, 25–58.

Roveri, M., Lugli, S., Manzi, V., Gennari, R., Schreiber, B.C., 2014b. High-resolution strontium isotope stratigraphy of the messinian deep mediterranean basins: implications for marginal to central basins correlation. Mar. Geol. 349, 113–125.

Sheppard, S.M.F., Schwarcz, H.P., 1970. Fractionation of carbon and oxygen isotopes and magnesium between coexisting metamorphic calcite and dolomite. Contrib. Mineral. Petrol. 26, 161–198.

Sofer, Z., 1978. Isotopic composition of hydration water in gypsum. Geochim. Cosmochim. Acta 42, 1141–1149.

Speranza, G., Cosentino, D., Tecce, F., Faccenna, C., 2013. Paleoclimate reconstruction during the Messinian evaporative drawdown of the Mediterranean Basin: insights from microthermometry on halite fluid inclusions. Geochem. Geophys. Geosyst. 14, 5054–5077.

Spötl, C., Vennemann, T.W., 2003. Continuous-flow isotope ratio mass spectrometric analysis of carbonate minerals. Rapid communications in mass spectrometry. RCM 17, 1004–1006.

Topper, R.P.M., Meijer, P.T., 2013. A modeling perspective on spatial and temporal variations in Messinian evaporite deposits. Mar. Geol. 336, 44–60.

Turchyn, A.V., Schrag, D.P., 2004. Oxygen isotope constraints on the sulfur cycle over the past 10 million years. Science (New York, NY) 303 (5666), 2004–2007.

Vasconcelos, C., McKenzie, J.A., Bernasconi, S., Grujic, D., Tiens, A.J., 1995. Microbial mediation as a possible mechanism for natural dolomite formation at low temperatures. Nature 377, 220–222.

Vasconcelos, C., McKenzie, J.A., 1997. Microbial mediation of modern dolomite precipitation and diagenesis under anoxic conditions (Lagoa Vermelha, Rio de Janeiro, Brazil). J. Sediment. Res. 67, 378–390.

Vasconcelos, C., McKenzie, J.A., Warthmann, R., Bernasconi, S.M., 2005. Calibration of the $\delta^{18}O$ paleothermometer for dolomite precipitated in microbial cultures and natural environments. Geology 33 (4), 317–320.